RESEARCH ARTICLE

MATERIALS SCIENCE

Hybrid solid electrolyte enabled dendrite-free Li anodes for high-performance quasi-solid-state lithium-oxygen batteries

Jin Wang[1,2,†], Gang Huang[3,†], Jun-Min Yan[1], Jin-Ling Ma[2], Tong Liu[2], Miao-Miao Shi[1,2], Yue Yu[2], Miao-Miao Zhang[4], Ji-Lin Tang[4] and Xin-Bo Zhang[2,*]

[1]Key Laboratory of Automobile Materials, Ministry of Education, Department of Materials Science and Engineering, Jilin University, Changchun 130022, China; [2]State Key Laboratory of Rare Earth Resource Utilization, Changchun Institute of Applied Chemistry, Chinese Academy of Sciences, Changchun 130022, China; [3]Materials Science and Engineering, Physical Science and Engineering Division, King Abdullah University of Science and Technology, Thuwal 23955-6900, Saudi Arabia and [4]State Key Laboratory of Electroanalytical Chemistry, Changchun Institute of Applied Chemistry, Chinese Academy of Sciences, Changchun 130022, China

ABSTRACT

The dendrite growth of Li anodes severely degrades the performance of lithium-oxygen ($Li-O_2$) batteries. Recently, hybrid solid electrolyte (HSE) has been regarded as one of the most promising routes to tackle this problem. However, before this is realized, the HSE needs to simultaneously satisfy contradictory requirements of high modulus and even, flexible contact with Li anode, while ensuring uniform Li^+ distribution. To tackle this complex dilemma, here, an HSE with rigid $Li_{1.5}Al_{0.5}Ge_{1.5}(PO_4)_3$ (LAGP) core@ultrathin flexible poly (vinylidene fluoride-hexafluoropropylene) (PVDF-HFP) shell interface has been developed. The introduced large amount of nanometer-sized LAGP cores can not only act as structural enhancer to achieve high Young's modulus but can also construct Li^+ diffusion network to homogenize Li^+ distribution. The ultrathin flexible PVDF-HFP shell provides soft and stable contact between the rigid core and Li metal without affecting the Li^+ distribution, meanwhile suppressing the reduction of LAGP induced by direct contact with Li metal. Thanks to these advantages, this ingenious HSE with ultra-high Young's modulus of 25 GPa endows dendrite-free Li deposition even at a deposition capacity of 23.6 mAh. Moreover, with the successful inhibition of Li dendrites, the HSE-based quasi-solid-state $Li-O_2$ battery delivers a long cycling stability of 146 cycles, which is more than three times that of gel polymer electrolyte-based $Li-O_2$ battery. This new insight may serve as a starting point for further designing of HSE in $Li-O_2$ batteries, and can also be extended to various battery systems such as sodium-oxygen batteries.

Keywords: lithium-oxygen batteries, dendrite suppression, Li anodes, hybrid solid electrolyte, LAGP, PVDF-HFP

INTRODUCTION

Recently, lithium-oxygen ($Li-O_2$) batteries have attracted wide attention because they have 10 times the theoretical energy densities of lithium-ion batteries. The $Li-O_2$ battery is composed of cathode, anode and electrolyte [1], among which, the widely used organic electrolyte (OE) is the most urgently in need of improvement owing to its security risk caused by Li dendrite and poor thermal safety [2–4]. Considering the high thermal stability and Li dendrite suppression ability of solid-state electrolyte, it has been regarded as the best alternative to OE in figuring out the issues of OE encountered [5].

The commonly used solid-state electrolyte can be broadly classified into two types: ceramic electrolyte (CE) and polymer electrolyte (PE). Although CE can offer good thermal stability, high Young's modulus and single ion conduction, the uneven contact between rigid CE and electrode hinders its successful use to produce high-performance batteries [6–9]. However, this is not a problem for PE because PE possesses outstanding flexibility and good wetting ability towards electrodes. What is more, the gel polymer electrolyte (GPE) obtained by adding plasticizer to PE holds good ionic conductivity and stability with Li anode [10,11]. As a result, poly (vinylidene fluoride-hexafluoropropylene) (PVDF-HFP)-based GPE, a representative GPE, has been widely used in $Li-O_2$ batteries due to its good stability and processability compared to other GPEs

*Corresponding author. E-mail: xbzhang@ciac.ac.cn
†Equally contributed to this work.

[12,13]. Unluckily, the disordered ion distribution and the intrinsic softness of the GPE make it useless in stopping Li dendrite formation during longterm cycling [14,15]. Since both CE and GPE alone cannot meet all the requirements of a perfect solidstate electrolyte, naturally, hybrid solid electrolyte (HSE), which can combine the advantages of CE and GPE, is promising to further promote the performance of the electrolyte, and has received extensive interest.

Although there are some HSEs that have been used in Li-O_2 batteries, the ability of these HSEs for inhibiting dendritic Li growth is still poor due to their negligence of modulus and nonuniform Li$^+$ distribution [16–20]. It is widely accepted that high Young's modulus and homogeneous Li$^+$ distribution are the key points in realizing dendrite-free Li deposition [21,22]. Therefore, to achieve dendrite-free Li deposition in the semiopen system of Li-O_2 batteries, HSE must meet the following conditions simultaneously: (i) the introduced rigid CE with three-dimensional ion transport channels must cover the whole surface of Li metal to ensure uniform Li$^+$ distribution and high modulus [23,24], (ii) the HSE should be soft and smooth enough to ensure good contact with Li metal, (iii) the distribution of GPE and CE in the HSE should be homogeneous to avoid local disorder of Li$^+$ [25–28], and (iv) the HSE should be O_2 or air stable [29]. Among all the available CEs, Na$^+$ superionic conductor (NASICON) type CE, represented by $Li_{1.5}Al_{0.5}Ge_{1.5}(PO_4)_3$ (LAGP), is the best candidate for constructing HSE because of its high stability in air. However, the LAGP cannot contact Li metal directly due to the reduction of Ge^{4+} by Li metal. Hence, a stable interface layer should be built between the Li metal and LAGP in HSE [30–33]. It is no doubt that there are contradictions among these requirements. Therefore, how to rationally design HSE to tackle the complex dilemma is difficult but necessary.

To meet the above requirements concurrently, herein an HSE with rigid core@ultrathin flexible shell interface has been designed by simply mixing nanometer-sized LAGP and a small amount of PVDF-HFP (Fig. S1a). As illustrated in Fig. 1, the low content of PVDF-HFP makes it form an ultrathin flexible shell on the surface of the rigid LAGP core. This ultrathin flexible shell can provide soft contact between the LAGP core and Li metal without affecting the Li$^+$ distribution near the Li metal, and suppress the Ge^{4+} reduction induced by direct contact with Li metal. The large number of nanometer-sized LAGP cores ensures that the entire Li metal surface is in close contact with the CE, providing uniform distribution of Li$^+$ and high Young's
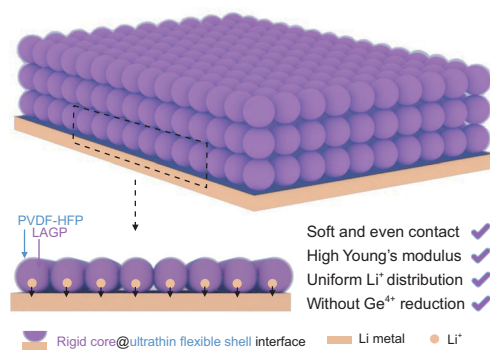

Figure 1. Schematic representation of dendrite-free lithium deposition enabled by HSE.

modulus. Based on this unique core@shell interface of HSE, dendrite-free Li deposition has been achieved both in symmetric batteries and quasisolid-state Li-O_2 batteries, as a result, prolonging the cycling life of the quasi-solid-state Li-O_2 battery.

RESULTS AND DISCUSSION

The ratio of PVDF-HFP/LAGP and the size of LAGP used in preparation of HSE have a strong impact on the core@shell interface. Therefore, we have set up three comparison groups (HSE-I with high-content, micro-sized LAGP; HSE-II with low-content, nanometer-sized LAGP; GPE without LAGP) to study how the core@shell interface works.

As shown in Fig. 2a, the surface of HSE is relatively flat and smooth. This advantage allows HSE to maintain a close and even contact with the electrode. The homogeneous distribution of the Ge element of LAGP, and the C and F elements of PVDF-HFP confirms that the LAGP and PVDF-HFP are mixed uniformly. Besides, the HSE has excellent flexibility (Fig. S1b), making it adapt well to the volume change of the electrode and be a promising candidate for constructing flexible quasi-solid-state batteries [34,35]. As indicated in Fig. S1c, the characteristic X-ray diffraction (XRD) peaks of the HSE are almost identical to those of LAGP powder, indicating that no undesirable reactions occurred during the solution-casting preparation process of the HSE. This can be further confirmed by the X-ray photoelectron spectroscopy (XPS) measurement (Fig. 2b), which shows that there is no Ge state change in the preparation process of the HSE, confirming the feasibility of the solutioncasting process (Fig. S2) [36]. For identification of the detailed structure of HSE, high resolution transmission electron microscopy (HRTEM) was performed. Figure 2c reveals that the LAGP core is wrapped by an ultrathin PVDF-HFP shell with a thickness of ∼5 nm. It is clear that the
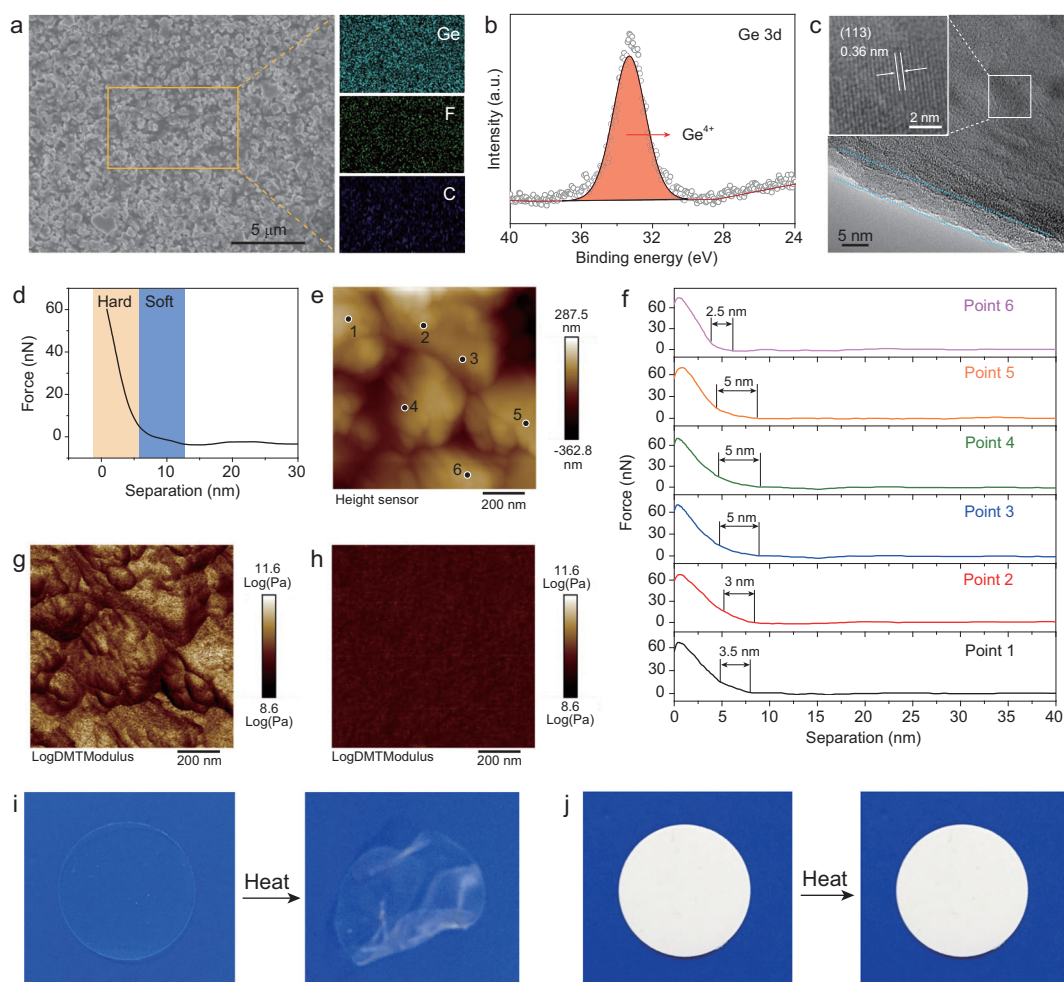
Figure 2. (a) Scanning electron microscope (SEM) image of HSE and the corresponding energy dispersive spectroscopy (EDS) mapping images of Ge, F and C elements. (b) Ge 3d XPS spectrum of HSE. (c) HRTEM image of HSE. (d) The force-separation curve of HSE. (e) AFM topography of HSE and (f) the corresponding force-separation curves of six points. Young's modulus mapping of (g) HSE and (h) GPE. Digital pictures of (i) GPE and (j) HSE before and after heating at 150°C for 5 min.

lattice fringes of LAGP display an interplanar spacing of 0.36 nm, matching well with the (113) plane of LAGP.

The thickness of the PVDF-HFP shell was further detected by atomic force microscopy (AFM). The force-separation curve consists of two parts with different slopes, indicating that the probe touches two different substances (Fig. 2d). The arc curve at the beginning of deformation corresponds to the typical deformation character of a soft sample, such as polymer. Then the curve changes from an arc to a straight line, suggesting that the probe touches hard LAGP. Therefore, the force-separation curve demonstrates that the surface of the LAGP is covered by an ultrathin layer of soft polymer. To prove that the LAGP core is completely wrapped by the PVDF-HFP shell, six more points were chosen on HSE to test their force-separation curves (Fig. 2e). As displayed in Fig. 2f, all these six points show similar curves with

an arc and a straight line, which confirms the uniformity and integrity of the core@shell interface of the HSE. Moreover, the force-separation curves also show that the thickness of the PVDF-HFP shell is around 5 nm, consistent with the HRTEM results. Electrochemical impedance spectra (EIS) measurement was then performed on HSE and LAGP pellet-based symmetric Li/Li batteries to check whether this ultrathin PVDF-HFP shell could improve the contact between the LAGP and Li metal electrodes (Fig. S3). The ionic conductivity of the LAGP pellet is 5.45×10^{-4} S cm^{-1} (Fig. S4), which is comparable to the reported result [33]. As shown in Fig. S5 and Table S1, with the introduction of the ultrathin shell, the interface resistance decreases by 185 times, indicating that the designed HSE could effectively improve the interfacial contact with the Li metal electrode, which is indispensable for guaranteeing the high performance of batteries.

By modulating the content and size of LAGP, we found that the morphology of the electrolyte changed significantly. Different to HSE, the surface of HSE-I is rough and rugged (Fig. S6), which would cause uneven contact between HSE-I and electrodes. AFM topography also confirms the more undulating surface of HSE-I than that of HSE (Figs 2e and S7), indicating that nanometer-sized LAGP can enable HSE with smooth surface and thus a good contact with electrodes. For HSE-II and GPE, smooth surfaces like HSE are observed (Fig. S8a and c). However, the main part of the HSE-II is PVDF-HFP, making the small portion of the LAGP form a discontinuous ion diffusion network, resulting in local disorder of Li^+ and poor modulus. In view of the mechanical strength of electrolyte being critical to suppress Li dendrite growth, the Young's modulus property of the HSE has been tested by AFM [37]. The mean Young's modulus value of the HSE is 25 GPa (Fig. 2g), which is the highest value in the reported hybrid solid electrolyte and even exceeds the values of those artificial inorganic interface layers (Table S2). In contrast, the GPE exhibits a mean Young's modulus value as low as 4.2 GPa, which is too soft to suppress Li dendrite growth (Fig. 2h) [38]. Figure 2i and j shows the digital pictures of the GPE and HSE, respectively. The GPE is transparent and colorless, while the HSE displays uniform white color due to the existence of numerous white nanometer-sized LAGP. Since the thermal safety is critical for Li-O$_2$ batteries, heat resistance tests for GPE, HSE, HSE-I and HSE-II have been performed. After being heated at 150°C for 5 minutes, the GPE is not flat anymore and exhibits a serious distortion (Fig. 2i). As indicated in Fig. S9, the HSE-I and HSE-II have obviously better thermal stabilities than that of GPE, but they still show some morphology change, indicating that the introduction of LAGP can to some extent improve the thermal stability of hybrid solid electrolyte. It is encouraging to note that the HSE experiences no shrinkage or decomposition after heat treatment (Fig. 2j), demonstrating its outstanding thermal stability. The higher thermal stability of HSE compared to that of HSE-I and HSE-II reveals that the thermal stability of hybrid solid electrolytes is closely related to the content and size of LAGP [39].

Considering that the ionic conductivity of electrolyte has a significant effect on the polarization of batteries, EIS of the synthesized electrolytes have been tested (Fig. S10). It is well known that the ionic conductivity is a product of Li^+ concentration and mobility, therefore the larger the content and the smaller the size of LAGP in the hybrid solid electrolyte, the higher the ion conductivity which can be obtained [40,41]. As a result, the HSE shows the highest ion conductivity, followed by HSE-I and HSE-II. The slightly lower ion conductivity of HSE-II compared to that of GPE is probably due to the relative rougher surface of HSE-II compared with GPE, making the transfer of Li^+ encounter more resistant. In addition to ionic conductivity, the electrochemical stability of electrolyte is also an important character for batteries to achieve good performance. As shown in Fig. S11, the HSE manifests a remarkably enhanced electrochemical oxidation window up to 5.2 V, which meets the requirement of Li-O$_2$ batteries. The worst electrochemical stability of HSE-I can be ascribed to its uneven and rugged surface, decreasing the effective contact area with Li metal. The large amount of PVDF-HFP in HSE-II makes it exhibit less stability than HSE, but HSE-II is still more stable than GPE due to the introduction of rigid LAGP.

In order to directly observe the effect of synthesized electrolytes on the morphology of lithium deposition, the Li-plating process was visualized by *in situ* optical microscopy. As shown in Fig. S12, Li dendrites rapidly nucleate and grow on the bare Li surface with plating time increasing. Although no dendrites can be detected on the GPE protected Li sheet at the beginning of deposition, Li dendrites emerge just after prolonging the plating time to one hour, and ultimately pierce the GPE as the deposition time increases. Dendrites are also formed on HSE-I and HSE-II protected Li sheets, but the morphology of the dendrites is different. Only a few dendrites appear on the HSE-I protected Li sheet, while the surface of the HSE-II protected Li sheet is completely covered by dendrites, probably due to the poor modulus induced by the insufficient amount of LAGP. In contrast, there is no dendrite forming on the HSE protected Li sheet during the whole plating process, indicating the effectiveness of the designed HSE for realizing dendrite-free Li deposition.

To further confirm the validity of the HSE in suppressing Li dendrite growth, symmetric Li/Li batteries with the synthesized electrolytes were built. It can be seen from Fig. 3a that the Li/Li battery with HSE shows the longest cycle life without obvious increase in voltage hysteresis. This excellent performance can be attributed to the high ion conductivity and dendrite-free Li deposition behavior endowed by the HSE. For HSE-I, the cycle life is much less than that of HSE, revealing that even and intimate contact between core@shell interface and Li metal is important for enabling long-term cycling stability. More interestingly, although HSE-II contains LAGP, its cycle life is even shorter than that of GPE. Therefore, the distribution of core@shell interface near the Li surface has a big effect on suppressing dendrite growth. As shown in the partially
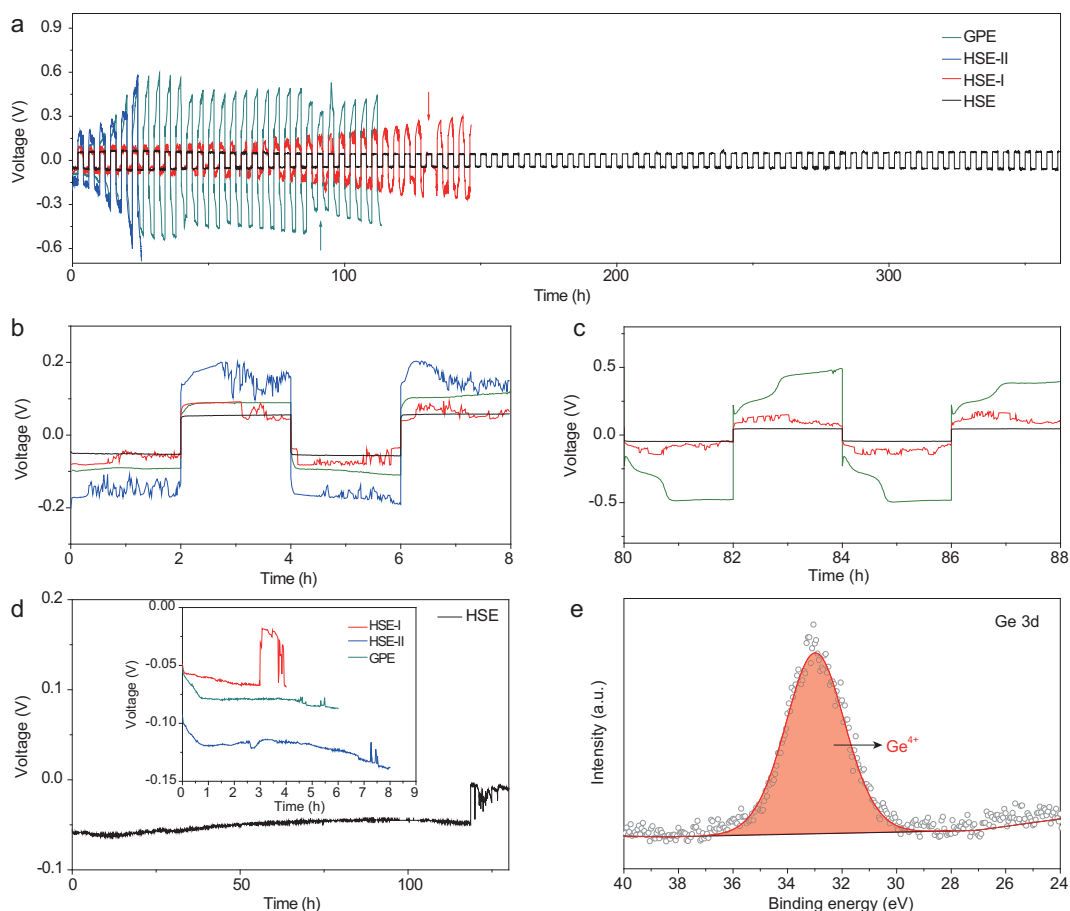
Figure 3. (a) Cycle life for symmetric Li/Li batteries with different electrolytes (current: 200 μA; each charge-discharge cycle length: 4 h). The arrows indicate short circuit. The magnified voltage profiles of (b) 0–8 h and (c) 80–88 h. (d) Li$^+$ depletion time tests in symmetric Li/Li batteries at 200 μA. (e) Ge 3d XPS spectrum of HSE disassembled from symmetric Li/Li battery after 30 cycles.

magnified voltage curves (Fig. 3b and c), the HSE with a relatively flat voltage plateau always exhibits the smallest polarization. Although the polarizations of the GPE and HSE-I are almost same at the beginning of cycling, the polarization of the GPE increases rapidly as the cycle goes on, which means the fast growth of Li dendrites. In contrast, the polarization of HSE-I manifests a much slower increase behavior, indicating that the growth of Li dendrites can be inhibited to some extent by its relatively high Young's modulus. For HSE-II, its poorest ion conductivity and low Young's modulus make it exhibit the largest polarization and shortest lifetime induced by the fast dendrite growth. Notably, except for HSE, the voltage curves of all the other electrolytes display obvious voltage fluctuation during cycling, implying unstable and non-uniform ion transfer. There is a slight difference in the voltage curves of the HSE-I and HSE-II. During each two hours of deposition, the voltage curve of the HSE-I begins to fluctuate at the later stage of deposition, while the voltage curve of the HSE-II fluctuates from the beginning of deposition. This phenomenon indicates that the

ion transfer of HSE-I is uniform and stable at the beginning, but turns to non-uniform and unstable as time increases, while the ion transfer of HSE-II is non-uniform and unstable all the time.

The causes of the long stability of the battery with HSE can be further identified by testing the Li$^+$ depletion time of the synthesized electrolytes-based symmetric Li/Li batteries. As shown in Fig. 3d, the Li$^+$ depletion time is determined by where the voltage curve apparently diverges due to the fast Li dendrite growth induced by complete Li$^+$ depletion [42]. The Li$^+$ consumption time of the synthesized electrolytes follows the sequence of HSE-I<GPE<HSE-II<HSE. The shortest Li$^+$ depletion time of HSE-I can be ascribed to its uneven contact with Li sheet, which would cause local Li$^+$ to be quickly depleted. Although the Li$^+$ depletion time decreases with the increase of the deposition current, the HSE always shows the longest depletion time and can still maintain 6 hours of stable Li plating at a high current of 500 μA (Figs S13 and S14), confirming that the designed HSE can effectively relieve Li$^+$ depletion
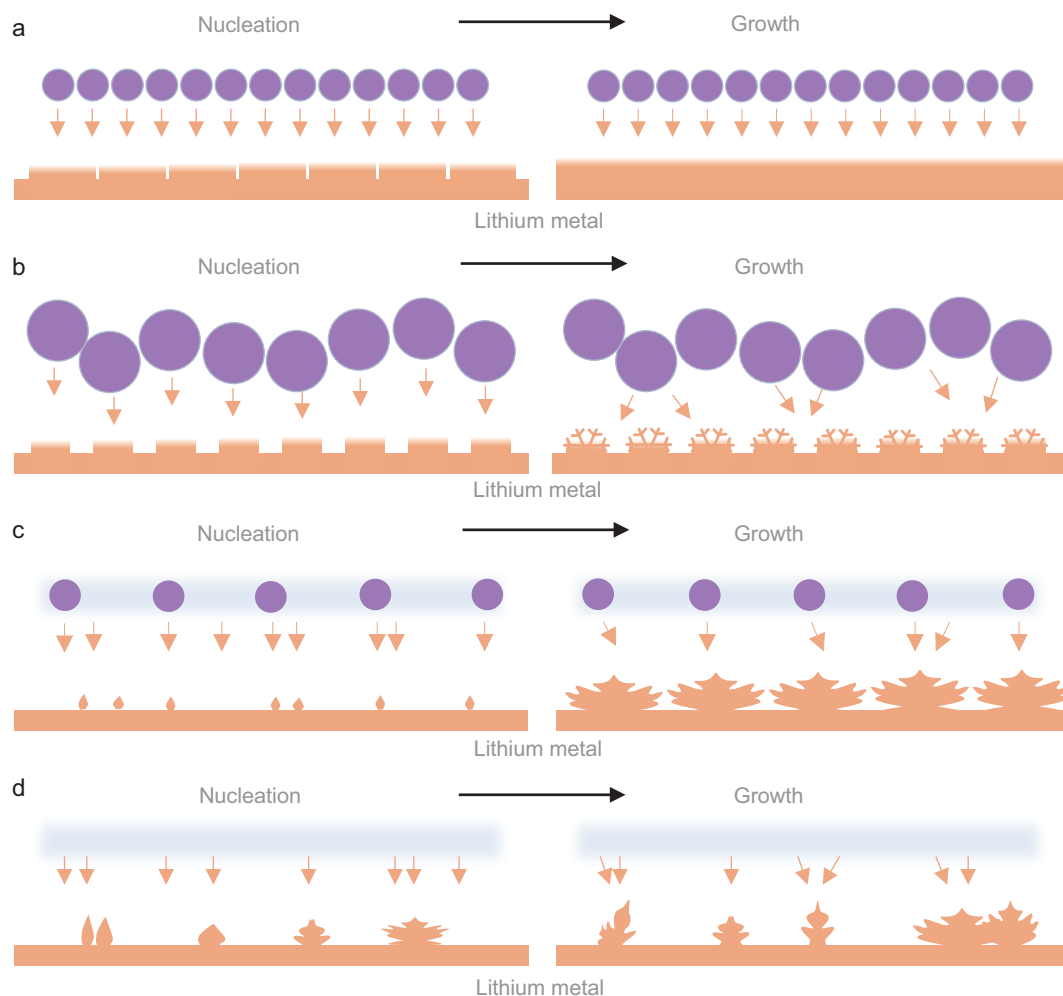
Figure 4. Schematic representation of Li deposition with (a) HSE, (b) HSE-I, (c) HSE-II and (d) GPE.

and inhibit Li dendrite growth. The strong dendrite inhibition ability of HSE can be further confirmed by the smooth and dendrite-free surface of Li sheet disassembled from symmetric HSE-based cells even at an ultra-high deposition capacity of 23.6 mAh. In contrast, Li sheets dissembled from symmetric Li/Li batteries with HSE-I/HSE-II/GPE are completely covered by Li dendrite even at lower deposition capacities (Figs S15–S17). In addition to Li$^+$ depletion, the chemical stability of LAGP is also worthy of attention. As shown in Fig. S18, when directly contacting the LAGP pellet with Li metal, two new peaks appear at 30 eV and 31.9 eV in the Ge 3d XPS spectrum, which can be attributed to Ge^0 and Ge^{2+}, respectively. In contrast, although the HSE endures 120 hours of cycling in battery, still only the Ge^{4+} peak can be detected (Fig. 3e), demonstrating that the ultrathin PVDF-HFP shell can effectively separate the LAGP core from the Li anode and avoid the Li metal induced Ge^{4+} reduction.

The Li deposition mechanism with different electrolytes is illustrated in Fig. 4. The rigid core@ultrathin flexible shell interface provides HSE with uniform Li$^+$ distribution, flexible and stable contact with Li sheet and high Young's modulus. Therefore, the Li$^+$ deposits evenly at the nucleation and growth stages (Fig. 4a). For HSE-I, the distribution of Li$^+$ is homogeneous initially, but the rough and rugged surface of HSE-I makes the ions in the locally uncontacted area with Li sheet quickly deplete, and as a result, the Li$^+$ deposits uniformly at the nucleation stage and dendrites appear in the later growth stage (Fig. 4b). The local disorder of Li$^+$ induced by the insufficient amount of LAGP in the HSE-II causes dendrite formation at the nucleation stage (Fig. 4c). As the deposition progresses, the local uneven distribution of Li$^+$ would be deepened and Li$^+$ would become less or be completely depleted, resulting in the rapid growth of a large number of dendrites. Although there is a good contact interface formed between the GPE and Li sheet, the uneven distribution of Li$^+$ results in the generation of dendrites, and the continuously formed dendrites will finally pierce
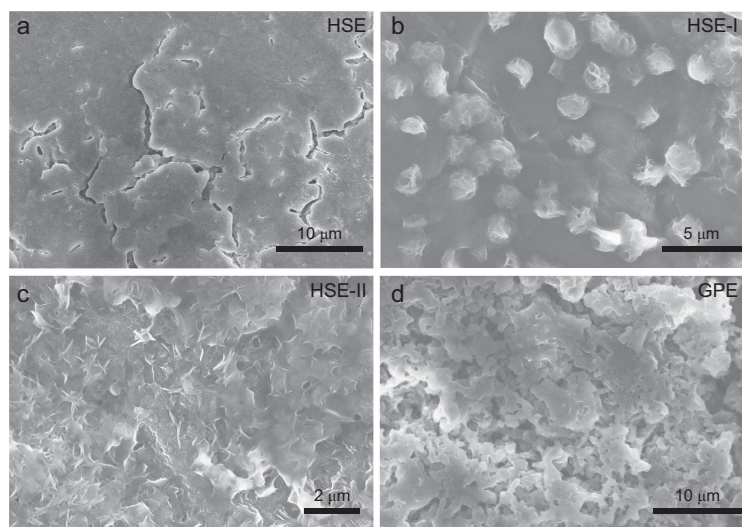
Figure 5. SEM images of Li sheets disassembled from symmetric batteries with (a) HSE, (b) HSE-I, (c) HSE-II and (d) GPE after cycling test.

into the soft GPE (Fig. 4d). In order to further verify our view, the morphology evolution of the different electrolytes protected lithium sheets after the cycling test was investigated by SEM (Fig. 5). Except for some cracks, no lithium dendrite can be discerned on the surface of the Li sheet taken from failed HSE-based battery (Fig. 5a). The cracks induced by the infinite volume change of Li during cycling may be the root of battery performance deterioration [43]. Although the HSE-I cannot completely rule out dendrite growth, only a small amount of sphere dendrites (later deposition) are produced on the initially formed dense Li layer (early deposition). Therefore, the cycle life of symmetric HSE-I-based battery is second to that of HSE-based battery (Fig. 5b). The ultrathin thickness of the dendrites on the HSE-II protected Li sheet surface leads to a strong tip electrical field, which would aggravate the dendrite growth. This is also an important reason for the worst performance of the HSE-II-based symmetric cell (Fig. 5c) [44]. For GPE-based battery, large and loose dendrites cover the Li sheet surface (Fig. 5d). These results demonstrate that the Li deposition behavior and the final morphology of lithium dendrites for the synthesized electrolytes are consistent with our expectations.

Inspired by the successful dendrite control through HSE with rigid core@flexible shell interface, HSE-based quasi-solid-state Li-O$_2$ batteries with Ru decorated-carbon nanotube (Ru-CNT) cathodes were assembled (Fig. S19). Figure 6a shows the discharge terminal voltage vs. cycle number profiles of the quasi-solid-state Li-O$_2$ batteries with different electrolytes cycled at a cutoff capacity of 1 000 mAh g^{-1} and a current density of 300 mA g^{-1}. Considering that the discharge ca-

pacity of carbon paper is quite limited [45], here, the capacity and current density are all based on the loading amount of active material: painted Ru-CNTs. It is clear that the HSE-based battery can realize 128 times stable cycling before the discharge terminal voltage reaching 2 V. In contrast, the discharge terminal voltages of the HSE-I, HSE-II and GPE-based batteries degrade to 2 V after only 60, 41 and 42 cycles, respectively. Since the loading amount of active materials has a significant effect on the battery life, the life of the HSE-based battery can be extended from 128 to 146 cycles by optimizing the loading amount of Ru-CNTs from 0.35 to 0.2 mg cm^{-2}. This improved life is comparable or superior to the reported works (Table S3). In order to figure out the impact of Li anodes on the quasi-solid-state Li-O$_2$ batteries during cycling, the discharge-charge curves at different cycles are shown in Fig. 6b–d. Regardless of the number of cycles, the HSE-based quasi-solid-state Li-O$_2$ batteries always exhibit the smallest charging (Li deposition process) over-potential and show no significant increase in over-potential as the cycle goes on, which is in sharp contrast to the other three electrolytes with rapid increase in charging over-potentials during cycling. The over-potential increase speed follows the sequence of HSE-II>GPE>HSE-I>HSE, which is consistent with the over-potential growth trend in symmetric Li/Li batteries. Suppressing dendrite growth can reduce the exposure of fresh lithium and then improve the anti-corrosion ability of Li sheets [46,47]. Therefore, the strong dendrite suppression ability of the HSE prolongs the lifetime of the quasi-solid-state Li-O$_2$ batteries. To visually observe the evolution of Li anodes in the quasi-solid-state Li-O$_2$ batteries, the morphology of Li anodes after 40 cycles was examined [48,49]. Unlike the initial smooth surface (Fig. S20), the morphology of the Li anodes changes after cycling. It can be seen from Fig. 6e that the Li anode in the HSE-based battery is still relatively dense and flat. On the contrary, the Li anodes in HSE-I, HSE-II and GPE-based batteries exhibit loose and porous structures and the morphology of the Li surface gets worse in the order of HSE-I, GPE and HSE-II (Fig. 6f–h). These loose and porous Li anodes hinder the transport of Li$^+$ and reduce the effective contact area with the electrolytes, thus increasing the impedance of the batteries and finally leading to the early death of the batteries. To further understand the underlying reasons for the above changes for Li anodes, the composition evolution of the cycled Li metals were examined by XRD. As shown in Fig. 6i, the Li anode in the HSE-based battery exhibits much lower LiOH peak intensity than that in other electrolytes-based batteries, revealing the least exposure surface of Li endowed by HSE. It is clear that the intensity
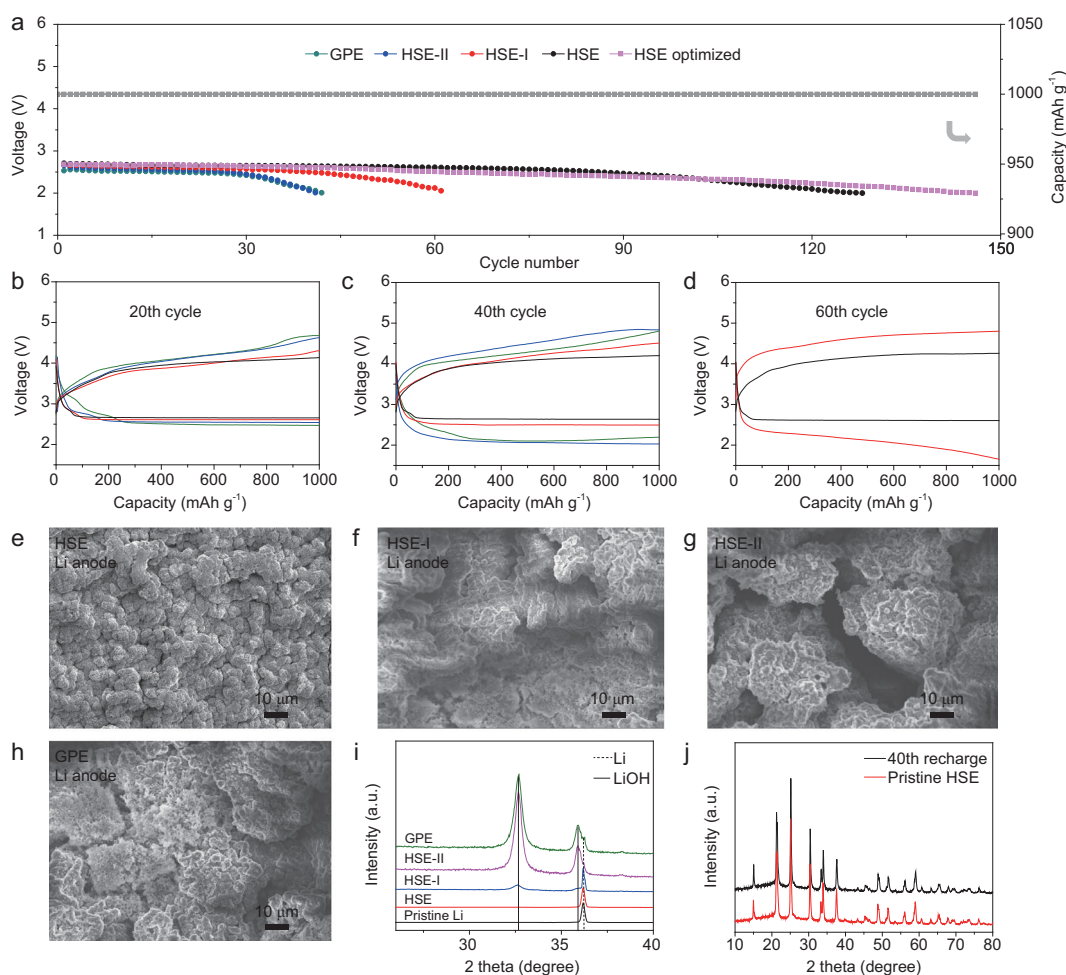
Figure 6. (a) The cycle life of quasi-solid-state Li-O$_2$ batteries with different electrolytes. The discharge-charge curves of quasi-solid-state Li-O$_2$ batteries at (b) 20th, (c) 40th and (d) 60th cycle. (e–h) SEM images and (i) XRD patterns of the Li anodes disassembled from quasi-solid-state Li-O$_2$ batteries after 40 cycles. (j) XRD patterns of the HSE before and after 40 cycles.

of the LiOH peak is inversely proportional to the ability of the electrolyte to suppress dendrites. Considering that the amount of LiOH on the Li metal surface can behave as an index to identify the corrosive degree of Li metal, these above findings substantially confirm that the suppression of Li dendrites can effectively alleviate Li corrosion, thereby improving battery performance. To explore the formation-decomposition processes of discharge products in quasi-solid-state Li-O$_2$ batteries with HSE, XRD and SEM were performed on the cathodes at different states. As shown in Fig. S21, only the peaks associated with Li$_2$O$_2$ are observed after discharging and these peaks disappear after subsequent recharging. Besides, it can be clearly seen that toroidal-like discharge products are well distributed along the Ru-CNTs (Fig. S22). After charging, these discharge products decompose completely. Therefore, HSE does not affect the reaction mechanism of Li-O$_2$ batteries which follows a typical Li$_2$O$_2$ formation-decomposition pathway.

What is more, HSE shows robust electrochemical stability which can be proved by the following SEM and XRD tests. As shown in Fig. S23, the HSE well maintains the compact morphology of the pristine HSE without any physical deterioration after 40 cycles, revealing the robustness of the HSE to withstand the rigorous cycling environment of a Li-O$_2$ battery. Besides, the corresponding XRD pattern of the cycled HSE is accordant with the pristine state, further testifying the excellent stability of HSE in the harsh oxidation environment during the cycling of a Li-O$_2$ battery (Fig. 6j).

Nowadays, electronics play an important role in our daily life. As the energy supply of those electronics, the safety of batteries should not be underestimated. Here, a cable-type HSE-based quasi-solid-state Li-O$_2$ battery has been assembled to check its heat resistance ability. As displayed in Fig. S24, even after heating and bending, this cable-type battery can still work normally on powering the red light-emitting diode display screen, indicating that

the HSE can successfully deal with the safety problems caused by thermal runaway. In contrast, the battery with GPE is short-circuited after heating due to the unsatisfactory thermal stability of GPE, highlighting the importance of a heat resistant electrolyte.

CONCLUSION

In summary, an ingenious HSE with rigid core@ultrathin flexible shell interface has been designed to realize dendrite-free Li deposition. In the HSE, each of the nanometer-sized LAGP core is wrapped by a soft PVDF-HFP shell with a thickness of ~5 nm. The ultrathin PVDF-HFP flexible shell provides soft and stable contact between the LAGP core and Li metal without affecting the Li$^+$ distribution near the Li sheet, and suppresses the reduction of LAGP core by Li metal. The large number of nanometer-sized LAGP cores afford uniform distribution of Li$^+$ and high Young's modulus. The synergistic interaction of the rigid LAGP core and the soft PVDF-HFP shell achieves excellent physical and chemical stability, uniform Li$^+$ distribution near Li metal, ultra-high Young's modulus of 25 GPa and good contact with electrodes, leading to dendrite-free Li deposition with a large deposition capacity up to 23.6 mAh. As a proof of concept application, the quasi-solid-state Li-O$_2$ battery with HSE shows a long cycle life of 146 cycles, and works normally even after heating treatment. This new insight may serve as a starting point for further design of hybrid solid electrolytes for Li-O$_2$ batteries, and can also be extended to various battery systems such as sodium metal batteries by substituting ion conductors.

METHODS

Preparation of HSE, HSE-I, HSE-II and GPE

Preparation of HSE was as follows: 0.7 g nanometer-sized LAGP powder was first well distributed in N-methyl-2-pyrrolidinone (NMP) under ultrasonic, then 0.3 g PVDF-HFP was added under stirring to obtain a stable sticky mixture. After this, the obtained mixture was casted on a glass plate by a doctor blade, and finally dried in a vacuum oven at 70°C for 24 h to obtain HSE membrane. The preparation process of HSE-I was similar to that of HSE, except nanometer-sized LAGP were changed to micro-sized LAGP. The same process as that of HSE was used to prepare HSE-II, except the ratio of nanometer-sized LAGP to PVDF-HFP was changed

from 7 : 3 to 3 : 7. The preparation process of GPE was similar to that of HSE, except without the addition of LAGP.

Characterizations

The material morphology was examined using a Hitachi S-4800 FE-SEM operating at 10 kV. Powder XRD tests were performed on a Bruker D8 Focus powder X-ray diffractometer using Cu Kα radiation. The tapping mode of AFM (Bruker Dimension Icon) was used to measure the morphology of samples. The mechanical properties mode of AFM was employed to test the force-separation curve and Young's modulus of samples. The probe model was RTESP-MPP-11100-10. Deflection sensitivity was 40.476 nm V^{-1}. Spring constant (k) was 50.4 N m^{-1}. Amplitude was 50 nm. f$_0$ was 327 kHz. Tip radius was 15.3 nm. EIS was tested with frequency ranging from 10^6 to 10^{-1} Hz at AC amplitude of 10 mV. The results were analyzed by Zview software. Linear sweep voltammetry (LSV) tests were measured on a BioLogic VMP3 electrochemical workstation with a scan rate of 1 mV s^{-1}. Transmission electron microscopy (TEM) was performed using an FEI Tecnai G2 S-Twin transmission electron microscope with a field emission gun operating at 200 kV. The stability of nanometer-sized LAGP against Li metal was checked by pressing a Li sheet on the surface of a LAGP pellet for 5 days. Then XPS analyses were carried out to check the surface of the LAGP pellet on an ESCALAB MKII X-ray photoelectron spectrometer. Ionic conductivity σ was calculated as $\sigma = \frac{l}{R \times S}$, where R represents the resistance, l represents the thickness of the electrolyte and S is the area.

Assembly of a quasi-solid-state Li-O$_2$ battery and electrochemical measurements

The as-synthesized electrolytes were activated with OE (1 M lithium triflate in tetraethylene glycol dimethyl ether). Each of the 2025 type quasi-solid-state Li-O$_2$ battery was assembled with Ru-CNTs cathode, activated quasi-solid-state electrolyte and Li anode (thickness: 0.4 mm; diameter: 14 mm) in an argon-filled glove box. All battery tests were carried out in the bottles full of pure O$_2$ at normal atmospheric pressure. Electrochemical performance measurements of the quasi-solid-state Li-O$_2$ cells were conducted on a LAND CT 2001A multi-channel battery testing system.

SUPPLEMENTARY DATA

Supplementary data are available at *NSR* online.

FUNDING

AUTHOR CONTRIBUTIONS

X.-B.Z., J.-M.Y., J.W. and G.H. developed the research concept. J.W. designed the electrolytes and conducted the electrochemical experiment. X.-B.Z., J.-M.Y., J.W., G.H., J.-L.M. and T.L. analyzed the experimental data and wrote the paper. J.W., M.-M.S., M.-M.Z. and J.-L.T. contributed to AFM characterizations. J.W. and Y.Y. performed *in situ* optical microscopy observations.

Conflict of interest statement. None declared.

REFERENCES

1. Meng XK, Liao KM and Dai J *et al.* Ultralong cycle life Li-O_2 battery enabled by a MOF-derived ruthenium-carbon composite catalyst with a durable regenerative surface. *ACS Appl Mater Interfaces* 2019; **11**: 20091–7.
2. Fan L, Wei S and Li S *et al.* Recent progress of the solid-state electrolytes for high-energy metal-based batteries. *Adv Energy Mater* 2018; **8**: 1702657.
3. Song K, Agyeman DA and Park M *et al.* High-energy-density metal-oxygen batteries: lithium-oxygen batteries vs sodium-oxygen batteries. *Adv Mater* 2017; **29**: 1606572.
4. Kim BG, Kim JS and Min J *et al.* A moisture and oxygen-impermeable separator for aprotic Li-O_2 batteries. *Adv Funct Mater* 2016; **26**: 1747–56.
5. Pang Q, Shyamsunder A and Narayanan B *et al.* Tuning the electrolyte network structure to invoke quasi-solid state sulfur conversion and suppress lithium dendrite formation in Li-S batteries. *Nat Energy* 2018; **3**: 783–91.
6. Wan J, Xie J and Mackanic D *et al.* Status, promises, and challenges of nanocomposite solid-state electrolytes for safe and high performance lithium batteries. *Mater Today Nano* 2018; **4**: 1–16.
7. Zhao C-Z, Zhang X-Q and Cheng X-B *et al.* An anion-immobilized composite electrolyte for dendrite-free lithium metal anodes. *Proc Natl Acad Sci USA* 2017; **114**: 11069–74.
8. Zhang H, Li C and Piszcz M *et al.* Single lithium-ion conducting solid polymer electrolytes: advances and perspectives. *Chem Soc Rev* 2017; **46**: 797–815.
9. Zhang J, Zang X and Wen H *et al.* High-voltage and free-standing poly (propylene carbonate)/$Li_{6.75}La_3Zr_{1.75}Ta_{0.25}O_{12}$ composite solid electrolyte for wide temperature range and flexible solid lithium ion battery. *J Mater Chem A* 2017; **5**: 4940–8.
10. Cheng X, Pan J and Zhao Y *et al.* Gel polymer electrolytes for electrochemical energy storage. *Adv Energy Mater* 2018; **8**: 1702184.
11. Zou XH, Lu Q and Zhong YJ *et al.* Flexible, flame-resistant, and dendrite-impermeable gel-polymer electrolyte for Li-O_2/air batteries workable under hurdle conditions. *Small* 2018; **14**: 1801798.
12. Shu C, Long J and Dou SX *et al.* Component-interaction reinforced quasi-solid electrolyte with multifunctionality for flexible Li-O_2 battery with superior safety under extreme conditions. *Small* 2019; **15**: 1804701.
13. Yin YB, Yang XY and Chang ZW *et al.* A water-/fireproof flexible lithium-oxygen battery achieved by synergy of novel architecture and multifunctional separator. *Adv Mater* 2018; **30**: 1703791.
14. Wu H, Cao Y and Su H *et al.* Tough gel electrolyte using double polymer network design for the safe, stable cycling of lithium metal anode. *Angew Chem Int Ed* 2018; **57**: 1361–5.
15. Liu F-Q, Wang W-P and Yin Y-X *et al.* Upgrading traditional liquid electrolyte via *in situ* gelation for future lithium metal batteries. *Sci Adv* 2018; **4**: 5383.
16. Le HT, Ngo DT and Kalubarme RS *et al.* Composite gel polymer electrolyte based on poly (vinylidene fluoride-hexafluoropropylene) (PVDF-HFP) with modified aluminum-doped lithium lanthanum titanate (A-LLTO) for high-performance lithium rechargeable batteries. *ACS Appl Mater Interfaces* 2016; **8**: 20710–9.
17. Ma Q, Zeng XX and Yue J *et al.* Viscoelastic and nonflammable interface design-enabled dendrite-free and safe solid lithium metal batteries. *Adv Energy Mater* 2019; **9**: 1803854.
18. Chen L, Li Y and Li S-P *et al.* PEO/garnet composite electrolytes for solid-state lithium batteries: from 'ceramic-in-polymer' to 'polymer-in-ceramic'. *Nano Energy* 2018; **46**: 176–84.
19. Wu S, Yi J and Zhu K *et al.* A super-hydrophobic quasi-solid electrolyte for Li-O_2 battery with improved safety and cycle life in humid atmosphere. *Adv Energy Mater* 2017; **7**: 1601759.
20. Cho SM, Shim J and Cho SH *et al.* Quasi-solid-state rechargeable Li-O_2 batteries with high safety and long cycle life at room temperature. *ACS Appl Mater Interfaces* 2018; **10**: 15634–41.
21. Wang C, Wang A and Ren L *et al.* Controlling Li ion flux through materials innovation for dendrite-free lithium metal anodes. *Adv Funct Mater* 2019; **29**: 1905940.
22. Monroe C and Newman J. The impact of elastic deformation on deposition kinetics at lithium/polymer interfaces. *J Electrochem Soc* 2005; **152**: A396–404.
23. Shen Y, Zhang Y and Han S *et al.* Unlocking the energy capabilities of lithium metal electrode with solid-state electrolytes. *Joule* 2018; **2**: 1674–89.
24. Cheng X-B, Zhao C-Z and Yao Y-X *et al.* Recent advances in energy chemistry between solid-state electrolyte and safe lithium-metal anodes. *Chem* 2019; **5**: 74–96.

25. Zhang C, Liu S and Li G *et al.* Incorporating ionic paths into 3D conducting scaffolds for high volumetric and areal capacity, high rate lithium-metal anodes. *Adv Mater* 2018; **30**: 1801328.

26. Zhang W, Nie J and Li F *et al.* A durable and safe solid-state lithium battery with a hybrid electrolyte membrane. *Nano Energy* 2018; **45**: 413–9.

27. Xu R, Zhang XQ and Cheng XB *et al.* Artificial soft-rigid protective layer for dendrite-free lithium metal anode. *Adv Funct Mater* 2018; **28**: 1705838.

28. Xiao W, Wang J and Fan L *et al.* Recent advances in $Li_{1+x}Al_xTi_{2-x}(PO_4)_3$ solid-state electrolyte for safe lithium batteries. *Energy Storage Mater* 2019; **19**: 379–400.

29. Zou XH, Liao KM and Wang D *et al.* Water-proof, electrolyte-nonvolatile, and flexible Li-air batteries via O_2-permeable silica-aerogel-reinforced polydimethylsiloxane external membranes. *Energy Storage Mater* 2020; **27**: 297–306.

30. Han X, Gong Y and Fu KK *et al.* Negating interfacial impedance in garnet-based solid-state Li metal batteries. *Nat Mater* 2017; **16**: 572–9.

31. Han F, Westover AS and Yue J *et al.* High electronic conductivity as the origin of lithium dendrite formation within solid electrolytes. *Nat Energy* 2019; **4**: 187–96.

32. Yan J, Yu J and Ding B. Mixed ionic and electronic conductor for Li-metal anode protection. *Adv Mater* 2018; **30**: 1705105.

33. Wang S, Wang J and Liu J *et al.* Ultra-fine surface solid-state electrolytes for long cycle life all-solid-state lithium-air batteries. *J Mater Chem A* 2018; **6**: 21248–54.

34. Yi J, Liu Y and Qiao Y *et al.* Boosting the cycle life of Li-O_2 batteries at elevated temperature by employing a hybrid polymer-ceramic solid electrolyte. *ACS Energy Lett* 2017; **2**: 1378–84.

35. Yi J and Zhou H. A unique hybrid quasi-solid-state electrolyte for Li-O_2 batteries with improved cycle life and safety. *ChemSusChem* 2016; **9**: 2391–6.

36. Liu Y, Li C and Li B *et al.* Germanium thin film protected lithium aluminum germanium phosphate for solid-state Li batteries. *Adv Energy Mater* 2018; **8**: 1702374.

37. Wang S, Liu Q and Zhao C *et al.* Advances in understanding materials for rechargeable lithium batteries by atomic force microscopy. *Energy Environ Sci* 2018; **1**: 28–40.

38. Li NW, Yin YX and Yang CP *et al.* An artificial solid electrolyte interphase layer for stable lithium metal anodes. *Adv Mater* 2016; **28**: 1853–8.

39. Zhai H, Xu P and Ning M *et al.* A flexible solid composite electrolyte with vertically aligned and connected ion-conducting nanoparticles for lithium batteries. *Nano Lett* 2017; **17**: 3182–7.

40. Zheng J and Hu Y-Y. New insights into the compositional dependence of Li-ion transport in polymer-ceramic composite electrolytes. *ACS Appl Mater Interfaces* 2018; **10**: 4113–20.

41. Zheng J, Tang M and Hu YY. Lithium ion pathway within $Li_7La_3Zr_2O_{12}$-polyethylene oxide composite electrolytes. *Angew Chem Int Ed* 2016; **55**: 12538–42.

42. Pang Q, Liang X and Shyamsunder A *et al.* An *in vivo* formed solid electrolyte surface layer enables stable plating of Li metal. *Joule* 2017; **1**: 871–86.

43. Ma JL, Meng FL and Yu Y *et al.* Prevention of dendrite growth and volume expansion to give high-performance aprotic bimetallic Li-Na alloy-O_2 batteries. *Nat Chem* 2019; **11**: 64–70.

44. Salvatierra RV, López-Silva GA and Jalilov AS *et al.* Suppressing Li metal dendrites through a solid Li-ion backup layer. *Adv Mater* 2018; **30**: 1803869.

45. Xu JJ, Wang ZL and Xu D *et al.* Tailoring deposition and morphology of discharge products towards high-rate and long-life lithium-oxygen batteries. *Nat Commun* 2013; **4**: 2438.

46. Ye L, Liao M and Sun H *et al.* Stabilizing lithium into cross-stacked nanotube sheets with an ultra-high specific capacity for lithium oxygen batteries. *Angew Chem Int Ed* 2019; **58**: 2437–42.

47. Hong YS, Zhao CZ and Xiao Y *et al.* Safe lithium-metal anodes for Li-O_2 batteries: from fundamental chemistry to advanced characterization and effective protection. *Batteries Supercaps* 2019; **2**: 638–58.

48. Zhao C, Liang J and Sun Q *et al.* Ultralong-life quasi-solid-state Li-O_2 batteries enabled by coupling advanced air electrode design with Li metal anode protection. *Small Methods* 2019; **3**: 1800437.

49. Zhu X, Zhao T and Wei Z *et al.* A novel solid-state Li-O_2 battery with an integrated electrolyte and cathode structure. *Energy Environ Sci* 2015; **8**: 2782–90.